Electronic Structure and Spectroscopy of Manganese Catalase and Di-μ-oxo [$Mn^{III}Mn^{IV}$] Model Complexes

Daniel R. Gamelin,[1a] Martin L. Kirk,[1a] Timothy L. Stemmler,[1b] Samudranil Pal,[1c] William H. Armstrong,*[1c] James E. Penner-Hahn,*[1b] and Edward I. Solomon*[1a]

Contribution from the Department of Chemistry, Stanford University, Stanford, California 94305, The University of Michigan, Ann Arbor, Michigan 48109, and Boston College, Chestnut Hill, Massachusetts 02167

Received July 12, 1993®

Abstract: Electronic absorption and magnetic circular dichroism (MCD) spectra are presented for a series of structurally perturbed di-μ-oxo [$Mn^{III}Mn^{IV}$] dimers and for superoxidized *L. plantarum* manganese catalase and azide perturbed manganese catalase. The study of this series of dimers allows the characteristics (energy, sign, bandshape, and intensity) of each observed spectral feature to be determined and correlated throughout the series, leading to assignment of 10 transitions in the optical spectra. Resonance Raman enhancement profiles on Mn–oxo stretching vibrations in the models are also presented which assist in the assignment of the observed features. The similarities of the MCD spectra in this series indicate that the observed spectral features below 30 000 cm^{-1} are all characteristic of the di-μ-oxo [$Mn^{III}Mn^{IV}$] structural unit, and absorption intensity in these dimers is attributable largely to oxo-to-Mn(IV) charge transfer and Mn(IV) d-d transitions. Spectral variations within the series are associated with structural perturbations involving ancillary and additional bridging acetate ligation. These spectrostructural correlations provide insight into various aspects of bonding in these dimers. A near-IR MCD band with little corresponding absorption intensity is identified as the transition between Jahn–Teller split e_g orbitals of Mn(III). Its energy reflects the magnitude of Mn(III) tetragonal distortion and provides insight into structural contributions to the redox properties of these dimers. A decrease in spectral intensity is observed upon the addition of bridging acetate ligation and is associated with the concomitant core bending of ~20°. A molecular orbital description is presented to explain this intensity variation with core bending and additionally provides insight into the orbital nature of di-μ-oxo dimer superexchange interactions. MCD allows a detailed spectral comparison of the models with the protein data and reveals a one-to-one correlation in band energies and signs with reduced absorption and MCD intensity in the energy region below ~19 000 cm^{-1} being the predominant difference. From the spectrostructural correlations developed in the model studies, these results indicate the presence of a bent and likely tribridged di-μ-oxo [$Mn^{III}Mn^{IV}$] dimeric core in superoxidized manganese catalase. The application of MCD to superoxidized manganese catalase and a series of model complexes has allowed for electronic and geometric insight into this metalloenzyme and the di-μ-oxo [$Mn^{III}Mn^{IV}$] structural unit and provides a basis for future studies on this and other Mn cluster active sites.

Introduction

Manganese clusters are catalytically active in several metalloenzymes[2] including manganese catalase (MnCAT),[3] the water-oxidation catalyst (WOC)[4] of photosystem II, and possibly manganese ribonucleotide reductase.[5] These enzyme active sites have been studied using a variety of physical techniques including magnetic susceptibility,[6] EPR,[4,7] XAS,[4,8] ESEEM,[9] and ENDOR[10] in efforts to understand the electronic and geometric features which govern their biological reactivity. In parallel with these studies, numerous synthetic compounds have been reported as structural,[11,12] spectroscopic,[11,13] and functional[14] models of these active sites, allowing their comparison to small, well-characterized systems through correlation of physical observables.

® Abstract published in *Advance ACS Abstracts,* February 15, 1994.

(1) (a) Stanford University. (b) The University of Michigan. (c) Boston College.

(2) *Manganese Redox Enzymes*; Pecoraro, V. L., Ed.; VCH Publishers: New York, 1992.

(3) (a) Kono, Y.; Fridovich, I. *J. Biol. Chem.* **1983**, *258*, 6015–6019. (b) Barynin, V. V.; Grebenko, A. I. *Dokl. Akad. Nauk. S.S.S.R.* **1986**, *286*, 461–464. (c) Algood, G. S.; Perry, J. J. *J. Bacteriol.* **1986**, *168*, 563–567.

(4) Debus, R. J. *Biochim. Biophys. Acta* **1992**, *1102*, 269–352.

(5) Willing, A.; Follmann, H.; Auling, G. *Eur. J. Biochem.* **1988**, *170*, 603–611.

(6) Sivaraja, M.; Philo, J. S.; Lary, J.; Dismukes, G. C. *J. Am. Chem. Soc.* **1989**, *111*, 3221–3225.

(7) (a) Fronko, R. M.; Penner-Hahn, J. E.; Bender, C. J. *J. Am. Chem. Soc.* **1988**, *110*, 7554–7555. (b) Khangulov, S. V.; Barynin, V. V.; Antonyuk-Barynina, S. V. *Biochim. Biophys. Acta* **1990**, *1020*, 25–33. (c) Khangulov, S. V.; Barynin, V. V.; Voevodskaya, N. V.; Grebenko, A. I. *Biochim. Biophys. Acta* **1990**, *1020*, 305–310.

(8) (a) Waldo, G. S.; Fronko, R. M.; Penner-Hahn, J. E. *Biochemistry* **1991**, *30*, 10486–10490. (b) Waldo, G. S.; Yu, S.; Penner-Hahn, J. E. *J. Am. Chem. Soc.* **1992**, *114*, 5869–5870.

(9) DeRose, V. J.; Yachandra, V. K.; McDermott, A. E.; Britt, R. D.; Sauer, K.; Klein, M. P. *Biochemistry* **1991**, *30*, 1335–1341.

(10) Khangulov, S.; Sivaraja, M.; Barynin, V. V.; Dismukes, G. C. *Biochemistry* **1993**, *32*, 4912–4924.

(11) (a) Wieghardt, K. *Angew. Chem., Int. Ed. Engl.* **1989**, *28*, 1153–1172. (b) Thorp, H. H.; Brudvig, G. W. *New J. Chem.* **1991**, *15*, 479–490. (c) Que, L.; True, A. E. *Progress in Inorganic Chemistry*; Wiley & Sons: Lippard, S. J., Ed.; New York, 1990; Vol. 38, pp 97–200.

(12) Abbreviations used include the following: cyclam (1,4,8,11-tetraazacyclotetradecane); bipy (2,2′-bipyridine); phen (1,10-phenanthroline); tpen (*N,N,N′,N′*-tetrakis(2-pyridylmethyl)-1,2-ethanediamine); bpea (*N,N*-bis(2-pyridylmethyl)ethylamine); bispicen (*N,N′*-bis(2-pyridylmethyl)-1,2-ethanediamine). (a) Brewer, K. J.; Calvin, M.; Lumpkin, R. S.; Otvos, J. W.; Spreer, L. O. *Inorg. Chem.* **1989**, *28*, 4446–4451. (b) Plaskin, P. M.; Stoufer, R. C.; Natthew, M.; Palenik, G. J. *J. Am. Chem. Soc.* **1972**, *94*, 2121–2122. (c) Stebler, M.; Ludi, A.; Bürgi, H.-B. *Inorg. Chem.* **1986**, *25*, 4743–4750. (d) Pal, S.; Gohdes, J. W.; Wilisch, W. C. A.; Armstrong, W. H. *Inorg. Chem.* **1992**, *31*, 713–716. (e) Pal, S.; Armstrong, W. H. *Inorg. Chem.* in press. (f) Cooper, S. R.; Calvin, M. *J. Am. Chem. Soc.* **1977**, *99*, 6623–6630. (g) Wieghardt, K.; Bossek, U.; Zsolnai, L.; Huttner, G.; Blondin, G.; Girerd, J.-J.; Babonneau, F. *J. Chem. Soc., Chem. Commun.* **1987**, 651–653. (h) Goodson, P. A.; Glerup, J.; Hodgson, D. J.; Michelsen, K.; Pedersen, E. *Inorg. Chem.* **1990**, *29*, 503–508. (i) Oki, A. R.; Glerup, J.; Hodgson, D. J. *Inorg. Chem.* **1990**, *29*, 2435–2441. (j) Towle, D. K.; Botsford, C. A.; Hodgson, D. J. *Inorg. Chim. Acta* **1988**, *141*, 167–168. (k) Bashkin, J. S.; Schake, A. R.; Vincent, J. B.; Chang, H.-R.; Li, Q.; Huffman, J. C.; Christou, G.; Hendrickson, D. N. *J. Chem. Soc., Chem. Commun.* **1988**, 700–702. (l) Suzuki, M.; Tokura, S.; Suhara, M.; Uehara, A. *Chem. Lett.* **1988**, 447–480.

(13) Sheats, J. E.; Czernuszewicz, R. S.; Dismukes, G. C.; Rheingold, A. L.; Petrouleas, V.; Stubbe, J.; Armstrong, W. H.; Beer, R. H.; Lippard, S. J. *J. Am. Chem. Soc.*, **1987**, *109*, 1435–1444.

(14) (a) Larson, E. J.; Pecoraro, V. L. *J. Am. Chem. Soc.*, **1991**, *113*, 7809–7810. (b) Gelasco, A.; Pecoraro, V. L. *J. Inorg. Biochem.* **1993**, *51*, 323. (c) Mathur, P.; Crowder, M.; Dismukes, G. C. *J. Am. Chem. Soc.* **1987**, *109*, 5227–5233.

0002-7863/94/1516-2392$04.50/0

The best characterized Mn cluster active site is the superoxidized form of MnCAT. This non-heme catalase has been isolated from *L. plantarum*,[3a] *T. thermophilus*,[3b] and *T. album*[3c] bacteria and is involved in the catalytic disproportionation of H_2O_2 to form H_2O and O_2. EPR[7] and XAS[8] studies have determined that the manganese site active in this process undergoes 2e⁻ redox cycling between [$Mn^{II}Mn^{II}$] and [$Mn^{III}Mn^{III}$] forms and in addition may be further reversibly oxidized to an inactive superoxidized form. In particular, EPR[7] and XANES[8a] studies of superoxidized MnCAT indicate the presence of a binuclear [$Mn^{III}Mn^{IV}$] cluster possessing a well isolated $S = {}^1/_2$ ground state, while EXAFS[8b] reveals a short 2.67 Å Mn···Mn separation and suggests the presence of Mn–oxo bonding. These results, when compared to synthetic manganese dimers, implicate a di-μ-oxo core in the superoxidized site of MnCAT.

EXAFS and EPR data have additionally been reported for several Kok S_n states of the tetranuclear Mn cluster in the photosynthetic WOC.[4] These also reveal a short ~2.7 Å Mn···Mn separation and, in the S_2 state, a multiline EPR signal similar to those of di-μ-oxo [$Mn^{III}Mn^{IV}$] model complexes. The remarkable similarities[8b] between EXAFS and EPR data from MnCAT and the photosynthetic WOC suggest that the di-μ-oxo [$Mn^{III}Mn^{IV}$] core is a fundamental structural unit in many manganese clusters in biology.

Electronic absorption spectroscopy and related excited-state methods have proven to be sensitive and direct probes of ligand-metal bonding in several biological systems.[15] Although electronic absorption spectra have been reported for a variety of dimeric manganese model complexes,[11-13] little attention has been given to the visible absorption characteristics of MnCAT in any of its oxidation states.[3,7b] While general similarities in absorption spectra of the as-isolated mixture of MnCAT oxidation states and of μ-oxo di-μ-carboxylato Mn^{III}_2 dimers have been noted and presented as evidence for this type of structure in active MnCAT,[11,13] literature absorption data for pure superoxidized MnCAT[7b] bear little resemblance to the spectra of di-μ-oxo [Mn^{III}-Mn^{IV}] dimers. In this study, excited-state absorption and MCD spectroscopies are used to probe the Mn dimer site of superoxidized *L. plantarum* MnCAT. To interpret these results, a combination of absorption, MCD, and resonance Raman (RR) spectroscopies are applied to a series of di-μ-oxo [$Mn^{III}Mn^{IV}$] model complexes related through structural perturbations. These structural perturbations include variation of ancillary ligation from aliphatic to aromatic to mixed aliphatic/aromatic N-donors and in particular the introduction of an additional acetate bridge and the concomitant core bending of ~20°. A set of 10 bands are assigned which originate from and are characteristic of the di-μ-oxo [$Mn^{III}Mn^{IV}$] structure. Variation of these spectral features over the series of dimers can be correlated with the structural variations of the series, and the insight obtained from these spectrostructural correlations is applied to understanding the geometric and electronic structure of superoxidized MnCAT.

Experimental Section

Model complexes and protein samples were prepared as previously described.[8,12a-e] Di-μ-oxo [$Mn^{III}Mn^{IV}$] dimers studied include [Mn_2O_2-(cyclam)$_2$]$(ClO_4)_3$[12a] (aliphatic, dibridged), [Mn_2O_2(bipy)$_4$]$(ClO_4)_3$[12b] (aromatic, dibridged), [Mn_2O_2(phen)$_4$]$(ClO_4)_3$[12c] (aromatic, dibridged), [Mn_2O_2(OAc)(tpen)]$(ClO_4)_2$[12d] (aliphatic/aromatic, tribridged), and [Mn_2O_2(OAc)(bpea)$_2$]$(ClO_4)_2$[12e] (aliphatic/aromatic, tribridged). AzMnCAT was formed by addition of 100-fold excess NaN_3 to superoxidized MnCAT. Complete conversion to the superoxidized form was determined by EPR spin quantitation. MCD data for model complexes were obtained on polycrystalline samples dispersed in poly(dimethylsiloxane) mulling agent, and molar ellipticities quantified at 5.5 T, 1.8 K from 50:50 butyronitrile/propionitrile glasses. Model complex absorption data were collected both at room temperature in CH_3CN solution and at 8 K in poly(dimethylsiloxane) mulls. Due to solubility restrictions of [Mn_2O_2-(cyclam)$_2$]$^{3+}$, its molar ellipticities were quantified from a 50:50 H_2O/glycerol glass, and solution absorption data was obtained in H_2O. Protein absorption data were collected at room temperature in 50 mM phosphate buffer. Protein MCD data were obtained as 70:30 D-glycerol/D_2O 50 mM phosphate buffer glasses at pH = 7. MCD experiments were performed on JASCO J500 (UV–vis/NIR) and J200 (NIR) CD polarimeters equipped with custom Oxford Instruments magnetooptical cryostats in extended sample compartments, using photomultiplier (S20, UV–vis and S1 vis/NIR) and cryogenically cooled InSb (NIR) detection. All samples were checked for depolarization effects by comparing the CD signal of nickel nitrate before and after the sample. Absorption experiments were performed at room temperature using a Cary-17 spectrometer, and at liquid helium temperatures using a MacPherson or Cary-17 spectrometer equipped with a Janis cryostat. RR profiles on solid samples were obtained using Coherent Kr^+ and Ar^+ lasers with Princeton Instruments photodiode array detection. Raman scattering intensities were calibrated against the 983.6 cm⁻¹ scattering peak in K_2SO_4.

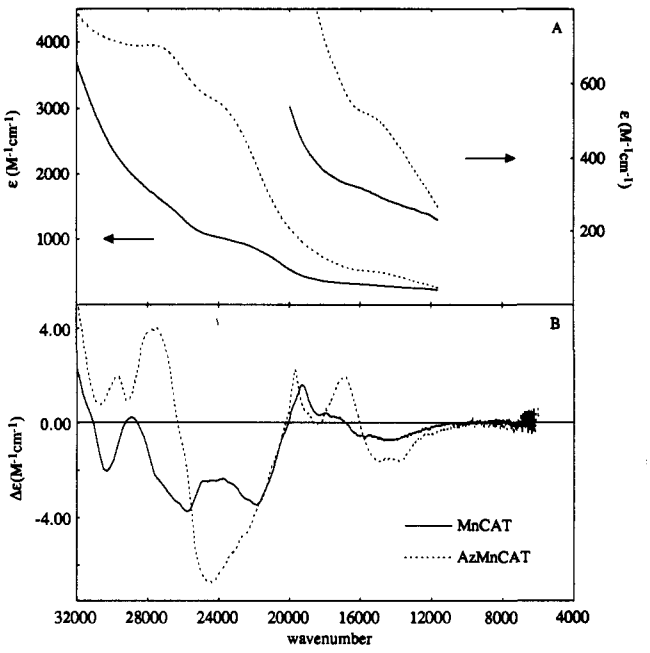

Figure 1. (A) 298 K absorption and (B) 1.8 K, 5.75 T MCD spectra of MnCAT and azide-perturbed MnCAT.

Results

Absorption spectra of pure superoxidized *L. plantarum* MnCAT and azide-perturbed superoxidized MnCAT (AzMnCAT) are shown in Figure 1a. The dominant spectral features of the absorption spectrum of MnCAT and AzMnCAT occur at energies greater than ~19 000 cm⁻¹. MnCAT exhibits discernible bands at 27 600 (1680 M^{-1} cm⁻¹), 22 650 (928 M^{-1} cm⁻¹), and 16 100 cm⁻¹ (320 M^{-1} cm⁻¹).[16] Azide-perturbed MnCAT exhibits features at 27 700 (3960 M^{-1} cm⁻¹), 24 000 (3100 M^{-1} cm⁻¹), and 15 200 cm⁻¹ (510 M^{-1} cm⁻¹).

Figure 1b presents the low-temperature MCD spectra of these same systems. There is a good correlation of band signs, energies, and shapes between the two MCD spectra, which may also be related to the observable features in the absorption spectra of Figure 1a. Apparent in the MCD of MnCAT are two strong negative bands at 25 770 (–3.75 M^{-1} cm⁻¹) and 21 870 cm⁻¹ (–3.46 M^{-1} cm⁻¹), a sharp positive band at 19 290 cm⁻¹ (1.59 M^{-1} cm⁻¹), and several weaker features at energies below 19 000 cm⁻¹. The MCD spectrum of azide-perturbed MnCAT exhibits a single, broad asymmetric band at 24 490 cm⁻¹ (–6.75 M^{-1} cm⁻¹), which appears to result from a shift toward one another of the 26 000

(15) See, for example: (a) Solomon, E. I., Lowery, M. D. *Science* **1993**, *259*, 1575–1581. (b) Zhang, Y., Gebhard, M. S., Solomon, E. I. *J. Am. Chem. Soc.* **1991**, *113*, 5162–5175.

(16) The previously reported[7b] absorption spectrum for superoxidized *T. thermophilus* MnCAT has two observable shoulders occurring at ~24 300 (~1650 M^{-1} cm⁻¹) and ~17 700 cm⁻¹ (~320 M^{-1} cm⁻¹).

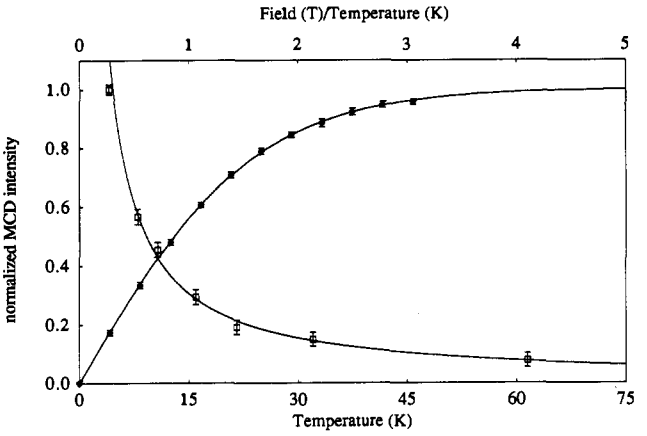

Figure 2. Variable-temperature (□) variable-field (♦) data for MnCAT MCD intensity.

and 22 000 cm^{-1} negative bands of MnCAT, and a sharp positive band at 19 700 cm^{-1} (2.20 M^{-1} cm^{-1}). Additionally, the azide perturbation leads to increased intensity in the low-energy region, with the original MnCAT bands at 17 000 and 14 320 cm^{-1} increasing from 0.12 to 1.95 M^{-1} cm^{-1} and –0.70 to –1.55 M^{-1} cm^{-1}, respectively.

Figure 2 shows the normalized MCD intensity of MnCAT plotted as a function of temperature, ranging from 4.3 to 62 K, and as a function of applied magnetic field, ranging from 0–5.5 T. The data shown are for intensity at 21 870 cm^{-1}, although identical results are obtained over the entire spectral region. The variable temperature data obey the Curie law (intensity increasing with $1/T$), demonstrating C-term MCD behavior. The variable-field data are fit using an $S = {}^1/_2$ hyperbolic tangent function with $g = 2.0$. These variable-temperature variable-field MCD experiments confirm the common $S = {}^1/_2$ ground-state origin of all observed bands. Similar results (data not shown) are obtained for azide perturbed MnCAT.

Figure 3a presents the room temperature solution absorption spectra of $[Mn_2O_2(cyclam)_2]^{3+}$ (planar Mn_2O_2 core) and $[Mn_2O_2(OAc)(tpen)]^{2+}$ (bent, tribridged $Mn_2O_2(OAc)$ core). Both complexes exhibit the two characteristic low-energy band maxima of di-μ-oxo $[Mn^{III}Mn^{IV}]$ systems at ~18 000 and ~15 400 cm^{-1}. Figure 3b relates the low-temperature solid-state MCD spectra of a series of representative di-μ-oxo dimers, $[Mn_2O_2(cyclam)_2]^{3+}$, $[Mn_2O_2(bipy)_4]^{3+}$, $[Mn_2O_2(phen)_4]^{3+}$, $[Mn_2O_2(OAc)(tpen)]^{2+}$, and $[Mn_2O_2(OAc)(bpea)_2]^{2+}$ to the absorption spectra of Figure 3a. These MCD spectra are simultaneously well fit over the entire series of complexes with a fixed set of 13 bands below ~30 000 cm^{-1}, corresponding to the minimum number of major observable positive and negative peaks in the MCD spectra. It is to be emphasized that these 13 bands are all required to be present on the basis of specific spectral features observed in Figure 3b. The simultaneous fit maintains identical widths, signs, and energy ordering for the set of 13 observed bands across the series of spectra, allowing only energies and intensities to vary. A representative fit is shown in Figure 4b for $[MnO_2(OAc)(tpen)]^{2+}$, where the parameters are also applied to the low-temperature solid-state mull absorption spectrum in Figure 4a. In contrast to the MCD fits, this Gaussian fit absorption spectrum is susceptible to baseline uncertainties from particle scattering effects. Gaussian fits of all model complex and protein MCD spectra are provided as supplementary material.

Band 1 is a weak negative feature ($\Delta\epsilon \approx -1$ M^{-1} cm^{-1}) occuring at very low energy and appears most prominently in the spectra (Figure 3b) of the bent-core complexes, $[Mn_2O_2(OAc)(tpen)]^{2+}$ (6000 cm^{-1}) and $[Mn_2O_2(OAc)(bpea)_2]^{2+}$ (8000 cm^{-1}), although it also appears to be present in $[Mn_2O_2(bipy)_4]^{3+}$ at 8000 cm^{-1} (on an expanded scale relative to Figure 3b). The positive band 2 ($\Delta\epsilon \approx +5$ M^{-1} cm^{-1}) in Figure 4b is observed clearly in several

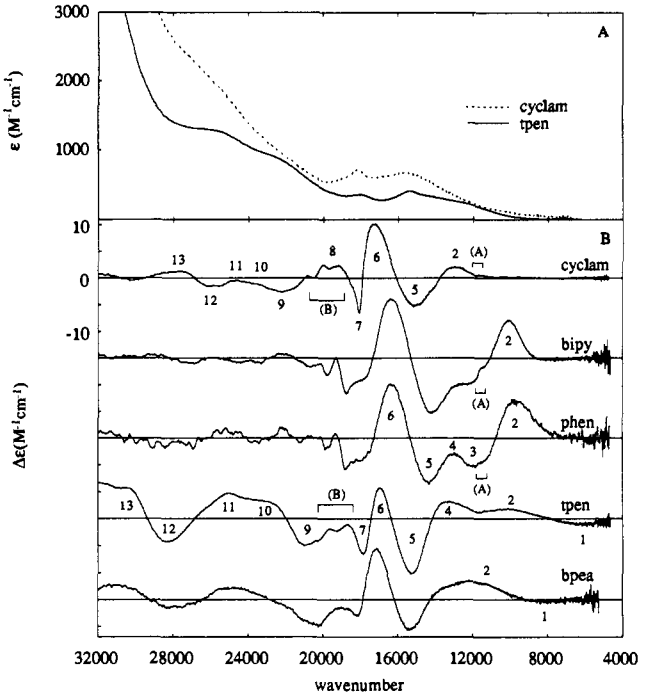

Figure 3. (A) 298 K solution absorption of $[Mn_2O_2(cyclam)_2]^{3+}$ and $[Mn_2O_2(OAc)(tpen)]^{2+}$ and (B) 1.8 K, 5.75 T MCD mull spectra of $[Mn_2O_2(cyclam)_2]^{3+}$, $[Mn_2O_2(bipy)_4]^{3+}$, $[Mn_2O_2(phen)_4]^{3+}$, $[Mn_2O_2(OAc)(tpen)]^{2+}$, and $[Mn_2O_2(OAc)(bpea)_2]^{2+}$. Numbers refer to Gaussian resolved spectral features discussed in the text.

of the MCD spectra of Figure 3b. Having little corresponding absorption intensity, band 2 appears very sensitive to ligation changes and is seen to shift from 12 900 cm^{-1} in $[Mn_2O_2(cyclam)_2]^{3+}$ to ~10 000 cm^{-1} in $[Mn_2O_2(bipy)_4]^{3+}$ and $[Mn_2O_2(phen)_4]^{3+}$. The negative band 3 is observed most clearly in $[Mn_2O_2(phen)_4]^{3+}$ at 11 900 cm^{-1} (–7 M^{-1} cm^{-1}). Band 4 is observed most clearly in $[Mn_2O_2(OAc)(tpen)]^{2+}$ (13 500 cm^{-1}, +3 M^{-1} cm^{-1}) but is also responsible, for example, for the positive turn at ~13 000 cm^{-1} in $[Mn_2O_2(phen)_4]^{3+}$ in Figure 3b. The series of alternating negative, positive, and negative bands 5 (~15 000 cm^{-1}, ~ –8 M^{-1} cm^{-1}), 6 (~17 000 cm^{-1}, ~10 M^{-1} cm^{-1}), and 7 (~18 000 cm^{-1}, ~ –10 M^{-1} cm^{-1}) are observed in all models and do not vary significantly in energy with variation of ancillary ligation. Band 8 in Figure 4b is a weak positive feature and is required by the positive intensity in $[Mn_2O_2(cyclam)_2]^{3+}$ at ~19 000 cm^{-1} (+2.5 M^{-1} cm^{-1}) in Figure 3b. Band 9 is a broad negative feature (~20 500 cm^{-1}, –5 M^{-1} cm^{-1}) and is seen in Figure 3b to decrease in energy from the cyclam to tpen and bpea complexes. Band 10 is observed clearly in the tpen complex (23 000 cm^{-1}, +4 M^{-1} cm^{-1}) and as a shoulder in the cyclam and bpea dimers. Bands 11, 12, and 13 are clearly observable in the cyclam, tpen, and bpea complexes. In the bipy and phen dimers dichroism above ~20 000 cm^{-1} drops significantly, and individual bands are not reliably identifiable. In addition to bands 1–13, two sets of weak sharp features are observed at ca. 12 000 and 20 000 cm^{-1} in all spectra of Figure 3b. These are labeled (A) and (B) in Figure 3b and are not included in the Gaussian fitting due to their limited contribution to the actual intensity. Note that overlapping oppositely signed MCD bands may result in artificial sharpness of features, such as in band 7, which overlaps heavily with the oppositely signed band 6.

From the Gaussian resolved absorption spectrum of $[Mn_2O_2(OAc)(tpen)]^{2+}$ in Figure 4a, bands 1 and 2 are seen to have little associated absorption intensity, while bands 3, 4, and 5 sum to form the lowest energy characteristic absorption band, where band 3 is that largely responsible for the NIR intensity discussed in ref 12f for the analogous $[Mn_2O_2(bipy)_4]^{3+}$ complex. Band

6, which is a dominant feature in the MCD spectrum, is very weak in absorption and corresponds to the minimum at 17 000 cm^{-1}. Band 7 is largely responsible for the higher of the two low-energy characteristic absorption features, and band 8 is weak and obscured. Band 9 is the first moderate intensity absorption feature, although it does not correspond to the summation maximum at 23 000 cm^{-1} in Figure 4a. Instead, the weaker band 10, situated between two similarly intense features, correlates best with the energy of the maximum. A series of bands (11, 12, and 13) with parameters determined from the MCD of Figure 4b combine to form the higher energy portion of the spectrum.

Low-temperature (8 K) solid-state absorption spectra of $[Mn_2O_2(OAc)(tpen)]^{2+}$ and $[Mn_2O_2(cyclam)_2]^{3+}$ are presented in Figure 5, along with the corresponding solid-state room-temperature RR profile data. Raman profiles were obtained for the totally symmetric Mn_2O_2 breathing mode[17] in the tpen (ν = 700 cm^{-1}), cyclam (ν = 679 cm^{-1}), and bipy (ν = 692 cm^{-1}, data not shown) dimers. These complexes display similar RR profiles, each having large maxima near 20 500 cm^{-1} (band 9) and dropping to minima between 20 000 and 17 000 cm^{-1} (bands 8, 7, and 6). Enhancement maxima occur at 20 500, 20 800, and 20 400 cm^{-1} in the tpen, cyclam, and bipy dimers, respectively. Each shows additional weaker enhancement below 16 000 cm^{-1} associated with the lower energy visible absorption feature composed of bands 5, 4, and 3. The RR profile for the bipyridine intraligand stretch (ν = 1495 cm^{-1}, data not shown) shows a sloping increase with increasing excitation energy. These data are fit to a Shorygin function[18] which yields a lower limit of ~25 000 cm^{-1} for the absorption feature associated with this Raman enhancement.

Discussion

The absorption spectrum of MnCAT in Figure 1a differs from those of the model dimers in its weak absorption below ~19 000 cm^{-1}, where two band maxima are characteristically observed in di-μ-oxo [$Mn^{III}Mn^{IV}$] dimers (Figure 3a). These absorption spectra are relatively nondescript, however, and a detailed analysis of the absorption data is precluded by overlapping bands and the paucity of resolved features. Alternatively, MCD spectroscopy applied to a series of di-μ-oxo [$Mn^{III}Mn^{IV}$] dimers reveals the presence of at least 13 distinct bands in the energy region below ~30 000 cm^{-1}, each with an associated energy, sign, magnitude, and bandshape, and these characteristics allow for the Gaussian resolved spectral features across the series of dimers studied. The quantitative spectral changes observed in this comparison reflect differences in Mn–oxo bonding and, when related to the known structural perturbations of the models, provide insight into the nature of Mn–oxo bonding in this biologically relevant class of molecules. We are thus interested in assigning each of the observed features, noting which are sensitive to the structural perturbations of the series, and making spectrostructural correlations based on these observations.

The similarities of the spectra presented in Figure 3 (shown Gaussian resolved in Figure 4 for $[Mn_2O_2(OAc)(tpen)]^{2+}$) indicate that the observable MCD and absorption features below ~30 000 cm^{-1} are all Mn_2O_2 core transitions. These include metal d-d, oxo-to-metal charge transfer (CT), and possibly intervalence transfer (IT) transitions (i.e., $Mn^{III} \rightarrow Mn^{IV}$ CT). The possibility of low-energy ancillary-ligand contributions (LMCT or π-π^*) is excluded by RR profiles on bipyridine intraligand stretching vibrations (ν = 1495 cm^{-1}) in $[Mn_2O_2(bipy)_4]^{3+}$, from which a lower limit of ~25 000 cm^{-1} is obtained. Previous assignments[12] of the observed absorption features (Figure 4a) in this class of molecules include band 7 as a Mn^{III} or Mn^{IV} d-d transition or an oxo-to-Mn^{IV} CT transition, Band 5 as an oxo-to-Mn^{III} or Mn^{IV} CT transition, and intensity in the 800-nm

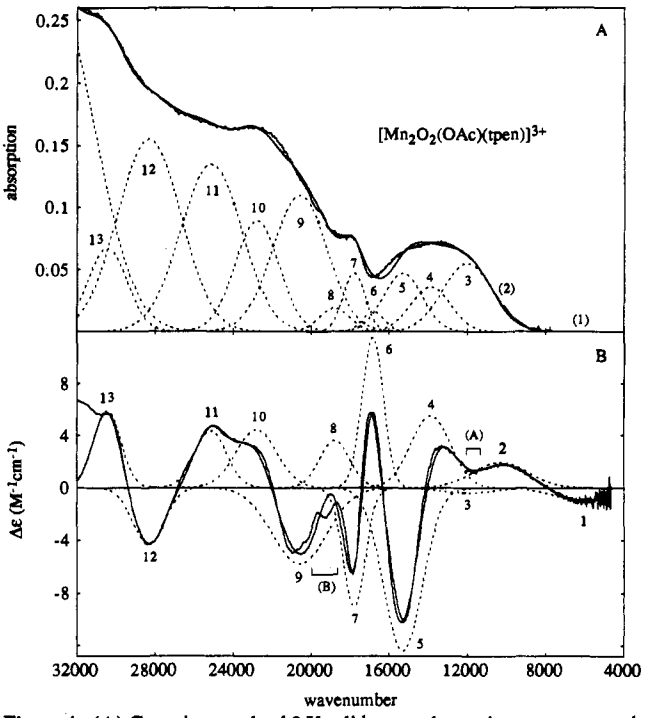

Figure 4. (A) Gaussian resolved 8 K solid-state absorption spectrum and (B) Gaussian resolved 1.8 K, 5.75 T solid-state MCD spectrum of $[Mn_2O_2(OAc)(tpen)]^{2+}$. The resulting fits are superimposed for comparison. Gaussian parameters used are based on simultaneous fits of a series of MCD spectra (see text).

(~12 500 cm^{-1}) region as an IT transition.[12a,f] It is noteworthy, however, that these mixed-valence spectra closely resemble those of their $Mn^{IV}_2O_2$ analogs,[12h,l] the latter having band maxima shifted to higher energies with significantly greater intensity, attributed to the presence of two Mn^{IV} ions. For example,[12h] $[Mn_2O_2(bispicen)_2]^{3+}$ has a broad maximum at 15 270 cm^{-1} (526 M^{-1} cm^{-1}) and a narrow peak at 18 063 cm^{-1} (568 M^{-1} cm^{-1}), while $[Mn_2O_2(bispicen)_2]^{4+}$ shows similar features at 15 867 cm^{-1} (730 M^{-1} cm^{-1}) and 18 446 cm^{-1} (951 M^{-1} cm^{-1}). Alternatively, $Mn^{III}_2O_2$ species[19] have only low ϵ transitions occurring at ~21 900 (141–315 M^{-1} cm^{-1}) and ~17 900 cm^{-1} (≤249 M^{-1} cm^{-1}).[20] This comparison indicates that the low-energy absorption features observed in these mixed valence dimers are dominantly features characteristic of oxo-bound Mn^{IV}.

The RR profiles of the core breathing mode presented in Figure 6 provide further insight into the observed absorption and MCD features. These RR profiles display a large enhancement maximum at ~20 500 cm^{-1}, corresponding to band 9, with additional low-energy enhancement at and below ~15 500 cm^{-1}, corresponding to bands 5, 4, and 3. The specific nature of these transitions is addressed in more detail below. Other spectral features having similar intensity but not associated with RR enhancement are then ligand field in nature.

Band 7 in Figure 4 corresponds to the remaining visible absorption maximum. Comparison to $Mn^{IV}_2O_2$ spectra and observation of minimal Raman enhancement in this region leads to assignment of this band as a Mn^{IV} ligand field transition. As the dominant mechanism for d-d intensity enhancement in these systems is through mixing of ligand field excited states with low-energy oxo-to-Mn^{IV} CT excited states, Mn^{IV} ligand field transitions are expected to be more intense than Mn^{III} ligand field transitions.

(17) Czernuszewicz, R. S.; Dave, B.; Rankin, J. G. In *Spectroscopy of Biological Molecules*; Hesser, R. E., Girling, R. B., Eds.; 1991; pp 285–288.
(18) Clark, R. J. H.; Mitchell, P. D. *J. Mol. Spectrosc.* **1974**, *51*, 458–474.
(19) (a) Goodson, P. A.; Oki, A. R.; Glerup, J.; Hodgson, D. J. *J. Am. Chem. Soc.* **1990**, *112*, 6248–6254. (b) Goodson, P. A.; Hodgson, D. J. *Inorg. Chem.* **1989**, *28*, 3606–3608. (c) Kitajima, N.; Singh, U. P.; Amagai, H.; Osawa, M.; Moro-oka, Y. *J. Am. Chem. Soc.* **1991**, *113*, 7757–7758.
(20) Spectroelectrochemical experiments[12a] on $[Mn_2O_2(cyclam)_2]^{3+}$ support this observation.

The lowest spin allowed octahedral Mn^{IV} d-d transition is the $^4A_2 \rightarrow {}^4T_2$ transition, corresponding to a $(t_{2g}^3) \rightarrow (t_{2g}^2)(e_g)$ one-electron promotion, and is usually observed at higher energies in monomers.[21] The reduced energy of this transition observed in these dimers is associated with the di-μ-oxo perturbation on the Mn^{IV} ligand field, depicted in the d orbital splitting pattern of Figure 6. Note that an x,y rotated coordinate system (Figure 6) is used in this analysis. The strong field di-μ-oxo coordination in these complexes defines the xy-plane, orienting the Mn atomic z-axis perpendicular to the oxo–Mn–oxo plane. In C_{2v} symmetry a second axis (x) lies in plane and bisects the oxo–Mn–oxo angle. Using this coordinate system, the e set of metal d orbitals transforms in C_{2v} symmetry as $a_1(z^2)$ and $b_2(xy)$, while the t_2 set transforms as $a_1(x^2-y^2)$, $b_1(xz)$, and $a_2(yz)$. The energy splitting pattern in Figure 6 reflects the large perturbation effect of the strong field oxo ligands, and the ordering is a direct consequence of oxo interactions with the individual d orbitals. Thus, in the e_g set the d_{xy} orbital directed along the Mn–oxo bonds is greatly raised in energy relative to the d_{z^2} orbital perpendicular to the Mn–oxo plane. Similarly, the $d_{x^2-y^2}$ should be the highest energy of the t_{2g} set as it bisects in-plane the oxo–Mn–oxo angle with potentially strong overlap with the in-plane $Op_{x,y}$ orbitals. The d_{xz} orbital is raised in energy to a lesser degree as it bisects the oxo–Mn–oxo angle out-of-plane, with potential for π-type overlap with the out-of-plane Op_z orbitals. The d_{yz} orbital is lowest in energy as it has the least potential for interaction with the oxo ligands due to the <90° oxo–Mn–oxo angles in these complexes.

In the di-μ-oxo C_{2v} symmetry, the Mn^{IV} $^4T_2$ excited state splits into three components, described by the three multi-electron wave functions[22]

$$\Psi_1 = \frac{1}{2}[\sqrt{3}|(yz)(x^2-y^2)(z^2)| + |(yz)(x^2-y^2)(xy)|]$$

$$\Psi_2 = \frac{1}{2}[-\sqrt{3}|(x^2-y^2)(xz)(z^2)| + |(x^2-y^2)(xz)(xy)|]$$

$$\Psi_3 = -|(xz)(yz)(xy)|$$

where the $^4A_2$ ground state is described as

$$\Psi = -|(xz)(yz)(x^2-y^2)|$$

In the orbital splitting pattern of Figure 6, Ψ_1 is the lowest energy component of the octahedral $^4T_2$ excited state. The lowest energy Mn^{IV} d-d transition, band 7, is thus the $^4A_2 \rightarrow {}^4T_2(\Psi_1)$ transition. This transition corresponds to a $1e^-$ promotion from d_{xz} to a linear combination of the split e_g orbitals. To higher energy, band 10 is also fairly strong in absorption intensity but does not exhibit Raman enhancement (Figure 5a) and is therefore assigned as the Mn^{IV} $^4A_2 \rightarrow {}^4T_2(\Psi_2)$ d-d transition. This transition involves promotion of the d_{yz} electron to the same linear combination of split e_g orbitals. The transition to Ψ_3, involving a $1e^-$ promotion from $d_{x^2-y^2}$ to d_{xy}, is expected at highest energy due to the large oxo splitting of the e_g set. The energy difference between bands 7 and 10 ($\sim$5000 cm^{-1}) results from the d orbital splitting of the d_{xz} and d_{yz} orbitals (Figure 6) due to out-of-plane interactions and directly reflects the extent of oxo–Mn^{IV} out-of-plane π-bonding in these systems.

Also in this region of Figure 4 are bands 8 and 6, which cannot be attributed to Mn^{IV}. Both bands have low absorption intensity,

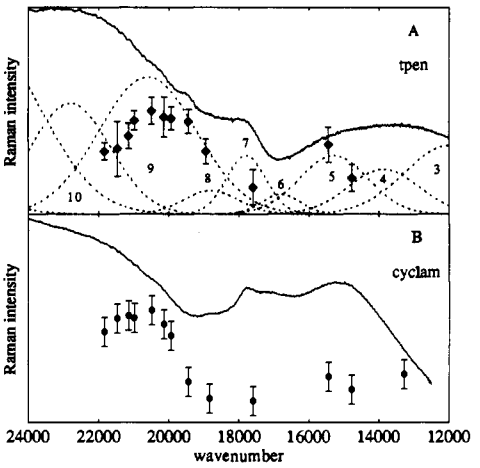

Figure 5. (A) 8 K solid-state absorption and 298 K 700 cm^{-1} resonance Raman scattering profile of $[Mn_2O_2(OAc)(tpen)]^{2+}$. Absorption Gaussians from Figure 4A are superimposed. (B) 8 K solid-state absorption and 298 K 679 cm^{-1} resonance Raman scattering profile of $[Mn_2O_2(cyclam)_2]^{3+}$.

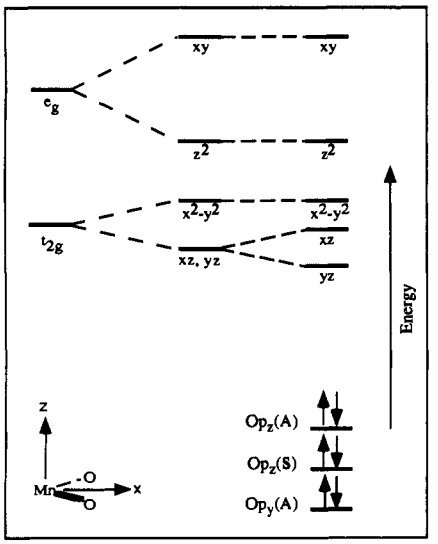

Figure 6. Qualitative ligand field splitting diagram indicating the effects of Mn–oxo interactions and C_{2v} symmetry on Mn d orbital energies. Metal d electrons are not included as this diagram is appropriate for both Mn^{III} and Mn^{IV} sites with four and three electrons, respectively, in separate d orbitals. The three highest energy Op orbital combinations are included (see text). Orbital labels are based on the (x,y rotated) coordinate system shown.

and band 6 in particular is strong in the MCD (large C_0/D_0 ratio[23]). These are assigned as Mn^{III} ligand field transitions. Two similar bands having low absorption intensity are reported for the homovalent $Mn^{III}_2O_2$ analogs[19] in this energy region. Octahedral Mn^{III} has one spin allowed d-d transition ($^5E_g \rightarrow {}^5T_{2g}$) corresponding to a $(t_{2g}^3)(e_g) \rightarrow (t_{2g}^2)(e_g^2)$ one-electron promotion. Upon reduction to C_{2v} symmetry in the Mn_2O_2 core these orbitals also split as depicted in Figure 6, with the e_g splitting enhanced by additional Jahn–Teller elongation along the z axis. This splitting leads to three possible spin allowed $d(t_2) \rightarrow d_{xy}(e)$ orbital transitions. We assign band 6 as the lowest energy of these, the $d_{x^2-y^2} \rightarrow d_{xy}$ ($^5B_2 \rightarrow {}^5A_1$) transition. Note that this transition, at $\sim$17 000 cm^{-1}, involves orbitals which only differ in their orientation in the xy plane and is therefore a measure of the equatorial 10Dq in these complexes. Band 8 is assigned as

(21) For example, at 21 800 cm^{-1} in MnF_6^{2-}, a σ,π donor system, and 31 950 cm^{-1} in $Mn(CN)_6^{2-}$, a σ donor/π acceptor system. Lever, A. B. P. *Inorganic Electronic Spectroscopy*, 2nd ed.; Elsevier Science Publishers B. V.: Amsterdam, The Netherlands, 1984; and references therein.

(22) Sugano, S.; Tanabe, Y.; Kamimura, H. *Multiplets of Transition-Metal Ions in Crystals*; Academic Press, Inc.: New York, 1970.

(23) Piepho, S. B., Schatz, P. N. *Group Theory in Spectroscopy, with Applications to Magnetic Circular Dichroism*; Wiley & Sons: New York, 1983.

Table 1. Comparison of Tetragonal Distortion, Jahn–Teller Splitting Energies, and Redox Potentials for $[Mn_2O_2(cyclam)_2]^{3+}$ and $[Mn_2O_2(bipy)_4]^{3+}$

	tetragonal distortion[a]	Jahn–Teller splitting (cm^{-1})[b]	III,III–III,IV[c]	III,IV–IV,IV[c]
$[Mn_2O_2(cyclam)_2]^{3+}$	1.141[d]	12 900	−0.12[d]	+1.00[d]
$[Mn_2O_2(bipy)_4]^{3+}$	1.067[e]	10 084	+0.29[f]	+1.25[f]

[a] Tetragonal distortion is reported as the ratio of Mn(III) axial and equatorial ancillary bond lengths, normalized to the same lengths on the Mn(IV) ion, i.e., (Mn^{III}ax/eq)/(Mn^{IV}ax/eq). [b] Band 2 from MCD. [c] V vs SCE. [d] Reference 12a. [e] Reference 12b. [f] Reference 12f.

the next highest Mn^{III} d-d, the $d_{xz} \rightarrow d_{xy}$ ($^5B_2 \rightarrow {}^5B_1$) transition, which is formally forbidden in C_{2v} symmetry but can gain intensity through reduced symmetry.

Interestingly, several transitions are observed in the near-IR. Absorption intensity in the region below band 5 has been previously assigned as resulting from an IT transition.[12a,f] IT transitions involve a metal-to-metal charge transfer and are thus unidirectionally polarized along the metal–metal vector. MCD C-term selection rules, however, require two perpendicular transition moments for an allowed transition.[23,24] Allowed in absorption, IT transitions are therefore expected to have small C_0/D_0 ratios. Although unidirectional transitions may gain limited MCD intensity through mixing with perpendicularly polarized transitions *via* spin-orbit coupling, the significant MCD intensities exhibited by bands 1–4 in Figure 3b suggest an alternative assignment for this low-energy region.

Salient in the low-energy MCD spectra of these dimers is band 2 (Figures 3b and 4), which has little associated absorption intensity (large C_0/D_0). The variation of band 2 throughout the series suggests a strong dependence of this transition energy on ancillary ligation and in particular on the magnitude of Mn^{III} tetragonal distortion. Table 1 correlates the tetragonal distortions of the Mn^{III} ion and the energies of band 2 from Figure 3b for $[Mn_2O_2(cyclam)_2]^{3+}$ and $[Mn_2O_2(bipy)_4]^{3+}$. These systems are well suited for comparison as each has identical axial and equatorial ancillary ligation. As seen in Table 1, the transition energy of band 2 correlates with the Mn^{III} axial elongation; band 2 occurs at higher energy in $[Mn_2O_2(cyclam)_2]^{3+}$, which has the greater tetragonal distortion. The large C_0/D_0 ratio and axial ligand dependence of band 2 lead to assignment of this transition as the Mn^{III} $^5B_2 \rightarrow {}^5A_1$ d-d transition resulting from Jahn–Teller splitting of the ^5E_g ground state. In d^4 systems, tetragonal distortion stabilizes the e_g electron by splitting the occupied and unoccupied e_g orbital energies (d_{z^2} and d_{xy} in Figure 6, respectively). This transition thus involves a $d_{z^2} \rightarrow d_{xy}$ one-electron promotion in Figure 6, and its energy is a function of the relative axial bond strength.

As the Jahn–Teller effect reflects energy stabilization of the Mn^{III} d_{z^2} electron in these systems, insight into the energetics of di-μ-oxo dimers is obtained through comparison of the Jahn–Teller stabilization energies observed in MCD to the redox potentials observed in cyclic voltammetry experiments. Each of the redox couples observed for these complexes (III,III–III,IV and III,IV–IV,IV) involves a Mn^{III} d_{z^2} orbital as the redox active orbital. The oxidation potentials therefore reflect the energy of the Mn^{III} d_{z^2} orbital. Table 1 compares the literature redox potentials for $[Mn_2O_2(cyclam)_2]^{3+}$ and $[Mn_2O_2(bipy)_4]^{3+}$, which indicate that $[Mn_2O_2(bipy)_4]^{3+}$ is significantly harder to oxidize than $[Mn_2O_2(cyclam)_2]^{3+}$ in both processes. This is in contrast to the relative Jahn–Teller d_{z^2} stabilization energies discussed above, indicating that donor sphere changes and their induced changes in the effective nuclear charge (Z_{eff}) on the Mn^{III} dominate over Jahn–Teller effects in determining Mn^{III} d_{z^2} ionization potentials.

(24) (a) Stephens, P. J. *Adv. Chem. Phys.* **1976**, *35*, 197–264. (b) Gerstman, B. S.; Brill, A. S. *J. Chem. Phys.* **1985**, *82*, 1212–1230.

In addition to the 13 transitions discussed above, a series of sharp weak MCD peaks (region B) are observed between 19 000 and 21 000 cm^{-1} in Figure 4b which appear invariable throughout the series shown in Figure 3b. Such features are indicative of ligand field independent spin flip transitions. In dimers, these spin forbidden transitions may gain limited intensity through exchange interactions. In this case, exchange enhancement of intensity will be greater for Mn^{III} spin flip transitions, as these become spin allowed (doublet to doublet) in the dimer. In addition, Mn^{III} spin flip transitions are generally expected to be higher in energy than the analogous Mn^{IV} transitions as a result of a nephelauxetic reduction in interelectronic repulsion upon increase of oxidation number. These bands are therefore assigned as Mn^{III} ligand field independent spin-forbidden ($^5B_2 \rightarrow {}^3\Gamma$) transitions. Similar but weaker features (region A in Figure 4b) are observed throughout the series at ~12 000 cm^{-1} in the MCD (Figure 3b) and are assigned as the Mn^{IV} ligand field independent spin-flip transitions ($^4A_2 \rightarrow {}^2\Gamma$). Sharp low intensity absorption features have been reported in this region for a number of dimeric Mn^{IV} complexes.[12h,l]

As discussed above, RR scattering profiles (Figure 5) on the Mn_2O_2 core breathing mode in these dimers reveal vibrational enhancement in two regions, a low-energy region (bands 5, 4, and 3) and at higher energy (band 9). The Raman enhancement and significant MCD intensities observed in these regions leads to assignment of these bands as oxo-to-Mn^{IV} CT transitions. In the di-μ-oxo core, the p orbitals of the two oxo ligands combine to form molecular orbitals which are symmetric (S) and antisymmetric (A) with respect to the *xz* plane bisecting the oxo–Mn–oxo angle (Figures 6 and 7). By symmetry, only one combination from each (S) and (A) pair will be involved in bonding to a particular metal d orbital and this will therefore be at deeper binding energy than its counterpart. For example, the $Op_z(S)$ MO shown in Figure 7 is of appropriate symmetry to interact with a Mn d_{xz} orbital, resulting in $Op_z(S)$ energetic stabilization, while the $Op_z(A)$ (not shown) is nonbonding by symmetry. Of the possible oxo combinations, three ($Op_z(S)$, $Op_z(A)$, and $Op_y(A)$) are expected to be at low binding energy, while three ($Op_y(S)$, $Op_x(S)$, and $Op_x(A)$) are more strongly bonding and thus deeper in energy. The former three are included in the energy diagram in Figure 6, where the $Op_z(S) \rightarrow Mn^{IV}$ CT transitions are higher in energy than the corresponding $Op_z(A) \rightarrow Mn^{IV}$ CT transitions. The $Op_y(A)$ orbital is estimated in Figure 6 to be deeper in energy than the Op_z orbitals due to bonding overlap with the Mn^{IV} d_{xy} orbital.[25]

The absorption intensities of these oxo $\rightarrow Mn^{IV}$ CT transitions derive from mixing of the oxo p and metal d orbitals involved in the CT transition. More specifically, the CT intensities are determined largely by the magnitude of the CT donor orbital (Op_D) character mixed into the CT acceptor orbital, which is predominantly a Mn^{IV} d orbital (d_A). This mixing is determined by the sum of $Op_D(S)$ and $Op_D(A)$ orbital overlap with the specific Mn^{IV} d_A orbital (one of which will be zero by symmetry). The two oxo $\rightarrow Mn^{IV}$ CT transitions, $Op_D(S) \rightarrow Mn^{IV}$ d_A and $Op_D(A) \rightarrow Mn^{IV}$ d_A, should therefore have similar absorption intensities as both intensities are determined by the same quantity, namely the magnitude of Op_D character mixed into the Mn^{IV} d_A orbital.

From the oxo combination MOs in Figure 6, five low-energy oxo $\rightarrow Mn^{IV}$ CT transitions should have significant absorption intensity based on the above overlap considerations, and these are associated with bands 9, 5, 4, 3, and 1. The specific transitions (and their band assignments, *vide infra*) are listed in Table 2. Of

(25) Extended Hückel calculations on di-μ-oxo [$Mn^{IV}Mn^{IV}$] dimers predict $Op_y(A)$ to be the highest energy oxo orbital combination due to the antibonding interaction of the two Op_y orbitals. This would also be consistent with our analysis of the observed CT transitions (*vide infra*), as the Mn^{IV} $d_{x^2-y^2}/d_{xz,yz}$ splitting due to the strong bonding interaction of $d_{x^2-y^2}$ with the $Op_y(S)$ ligand combination is expected to be far greater than the $Op_z(A,S)/Op_y(A)$ splitting. Proserpio, D. M.; Hoffmann, R.; Dismukes, G. C. *J. Am. Chem. Soc.* **1992**, *114*, 4374–4382.

Table 2. Spectral Assignments for Optical Features of Di-μ-oxo [$Mn^{III}Mn^{IV}$] dimers

band	assignment	type	energy region (cm^{-1})
1	$Op_z(A) \rightarrow Mn^{IV}d_{yz}$	CT	6500–8000
2	$Mn^{III}d_{z^2} \rightarrow d_{xy}$	d-d	9800–12 900
3	$Op_z(S) \rightarrow Mn^{IV}d_{yz}$	CT	11 500–13 000
4	$Op_z(A) \rightarrow Mn^{IV}d_{xz}$	CT	13 500
5	$Op_z(S) \rightarrow Mn^{IV}d_{xz}$	CT	14 000–15 500
6	$Mn^{III}d_{x^2-y^2} \rightarrow d_{xy}$	d-d	16 500–17 500
7	$Mn^{IV}\,{}^4A_2 \rightarrow {}^4T_2(\Psi_1)$	d-d	18 000
8	$Mn^{III}d_{xz} \rightarrow d_{xy}$	d-d	19 000
9	$Op_y(A) \rightarrow Mn^{IV}d_{x^2-y^2}$	CT	20 000–20 500
10	$Mn^{IV}\,{}^4A_2 \rightarrow {}^4T_2(\Psi_2)$	d-d	22 800
11			25 000–26 000
12			27 000–28 000
13			31 000
(A)	$Mn^{IV}\,{}^4A_2 \rightarrow {}^2\Gamma$	spin flip, d-d	11 600
(B)	$Mn^{III}\,{}^5E \rightarrow {}^3\Gamma$	spin flip, d-d	19 000–21 000

these five, four are $Op_z(A,S) \rightarrow Mn^{IV}d_{xz}$ and d_{yz} transitions, while the fifth is an $Op_y(A) \rightarrow Mn^{IV}d_{x^2-y^2}$ CT transition (Figure 6), involving distinct oxo and metal orbitals not involved in the other four transitions. Since the Op_y orbitals have no overlap with the metal d_{xz} and d_{yz} orbitals, transitions from $Op_y(A)$ to Mn^{IV} d_{xz} and d_{yz} should not be observed. Likewise, Op_z transitions to $d_{x^2-y^2}$ should not be observed due to the negligible overlap of these orbitals.

The $Op_y(A) \rightarrow Mn^{IV}d_{x^2-y^2}$ CT transition should be the most intense absorption band of the five as it involves more strongly overlapping orbitals. From Figure 4a, band 9 is the lowest energy relatively intense CT absorption feature and is therefore assigned as the $Op_y(A) \rightarrow Mn^{IV}d_{x^2-y^2}$ CT transition. The high energy of band 9 relative to bands 5, 4, 3, and 1 is a result of the stronger in-plane than out-of-plane bonding interactions of the Mn^{IV} $d_{t_{2g}}$ orbitals in these systems, also reflected in the $d_{x^2-y^2}/d_{xz,yz}$ t_{2g} splitting shown in Figure 6.

The four lower energy CT transitions all originate from the Op_z orbitals and are transitions to the d_{xz} and d_{yz} orbitals in Figure 6. As discussed above, the $Op_z(S) \rightarrow Mn^{IV}$ CT transitions are higher in energy than the corresponding $Op_z(A) \rightarrow Mn^{IV}$ CT transitions due to bonding. Additionally, due to the <90° oxo–Mn^{IV}–oxo angle in these dimers Op_z overlap is better with d_{xz} than with d_{yz}, and transitions to the d_{xz} orbital will generally have greater absorption intensity than those to d_{yz}. These observations lead to the assignment of bands 5 and 3 as the $Op_z(S) \rightarrow Mn^{IV}d_{xz}$ and d_{yz} CT transitions, respectively, and the lower energy weaker bands 4 and tentatively 1 as the $Op_z(A) \rightarrow Mn^{IV}d_{xz}$ and d_{yz} CT transitions, respectively. These transitions can gain MCD intensity through spin orbit coupling of the d_{xz} and d_{yz} orbitals, which are connected by the $\hat{L}_z$ operator. To higher energy, the next CT transition expected is the $Op_y(S) \rightarrow Mn^{IV}d_{x^2-y^2}$, and this is a possible assignment for either band 11, 12, or 13.[26]

The spectral features of di-μ-oxo [$Mn^{III}Mn^{IV}$] dimers have been assigned above in some detail and are summarized in Table 2. These assignments reveal that the features observed are directly related to bonding interactions in the di-μ-oxo core and as such provide a probe of oxo–Mn bonding in the di-μ-oxo unit.

Absorption intensities at energies <19 000 cm^{-1} diminish significantly upon going from the cyclam to tpen complexes (Figure 3a), correlating with di-μ-oxo core bending. This correlation appears to be general; literature values[27] for $\epsilon^{max}_{\sim 15400 cm^{-1}}$ in structurally characterized bent di-μ-oxo [Mn^{III}-Mn^{IV}] dimers range from 345[12g] to 440 M^{-1} cm^{-1},[12d] while for structurally characterized planar complexes this range is from 526[12h] to 1380 M^{-1} cm^{-1}.[12i] Since absorption intensity in this region is dominated by $Op \rightarrow Mn^{IV}d_{t_{2g}}$ CT transitions and Mn^{IV} d-d transitions which gain intensity through mixing with these CT excited states, this general reduction in intensity upon core bending must reflect a reduction in CT efficiency and hence in oxo–Mn overlap.

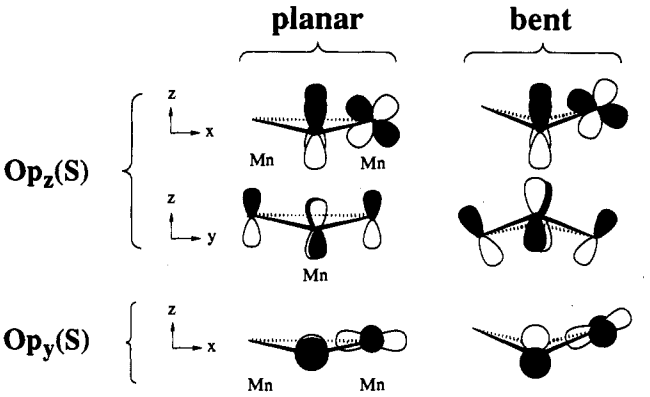

Figure 7. Molecular orbital scheme depicting the effects of di-μ-oxo core bending on Mn–oxo orbital overlap for the two interactions largely responsible for visible absorption intensity in di-μ-oxo [$Mn^{III}Mn^{IV}$] dimers (see text).

Figure 7 shows the effect of core bending on Op–$Mn^{IV}d_{t_{2g}}$ orbital overlap for the two orbital interactions responsible for the majority of visible absorption intensity (*vide supra*). Upon core bending, the out-of-plane Op_z orbitals tilt relative to the z-axis to remain perpendicular to the Mn–oxo–Mn plane, while the Mn^{IV} d_{xz} orbital rotates away from the converging Op_z lobes. Likewise, the in-plane Op_y orbitals rotate to remain in the Mn–oxo–Mn plane, while $d_{x^2-y^2}$ rotates with the oxo–Mn–oxo plane. The effect is thus a decrease in overlap of the metal and oxygen orbitals for both the Op_y–Mn^{IV} $d_{x^2-y^2}$ and Op_z–Mn^{IV} d_{xz} interactions upon core bending, resulting in decreased oxo $\rightarrow Mn^{IV}$ CT intensity.[28] This decrease in Op overlap with the Mn^{IV} d orbitals will result in reduced Op(S) and Op(A) $\rightarrow Mn^{IV}$ CT intensity as well as Mn^{IV} d-d intensity, which, as mentioned above, dominate the low-energy absorption spectra of di-μ-oxo [$Mn^{III}Mn^{IV}$] dimers. The higher energy region may be complicated by contributions from other chromophores. Interestingly, these same orbital interactions of Figure 7 should make significant superexchange contributions to the magnetic properties of these dimers, although to date there is insufficient literature data to clearly define this magneto-structural correlation.[29]

Figure 8 compares the MCD spectrum of a representative di-μ-oxo [$Mn^{III}Mn^{IV}$] model complex to those of superoxidized MnCAT and AzMnCAT. The features observed in the MCD spectra of MnCAT are qualitatively similar to those observed in the model complexes and are fit reasonably well to the same set of 13 Gaussians applied to the dimer series (see supplementary material). The one-to-one correlation of band energies and signs between the model and enzyme MCD spectra support the description of superoxidized MnCAT as a di-μ-oxo [$Mn^{III}Mn^{IV}$] dimer. In particular, similarities in the region of band 9 in the MCD spectra and the large Mn_2O_2 vibrational RR enhancement under this band in the models argue for similar Mn–oxo bonding. Absent from the MnCAT MCD spectra is the low-energy positive MCD band 2 observed in the models in Figure 3b and assigned as a Mn^{III} $d_{z^2} \rightarrow d_{xy}$ one-electron promotion resulting from Jahn–Teller splitting of the ^5E_g ground state. This absence is likely indicative of greater axial ligand field strength in the enzyme, resulting in a smaller tetragonal distortion.

(26) Several of these CT transitions display solvatochromism, as reported[12f] for near-IR absorption in $[Mn_2O_2(bipy)_4]^{3+}$.

(27) These values are not single band oscillator strengths and hence do not take into account the effects of variably overlapping bands in determining summation intensities.

(28) These observations are supported by extended Hückel calculations,[25] which suggest a net decrease in Mn–oxo overlap population with core bending in $Mn^{IV}{}_2O_2$ systems.

(29) There are exceptions to the expected trend in J values, most notably $[Mn_2O_2(OAc)(tmtacn)_2]^{2+}$ which is reported[12g] to have an unusually large J value of -220 cm^{-1} ($H = -2JS_1 \cdot S_2$); these exceptions implicate other contributions to magnetic exchange in these dimers.

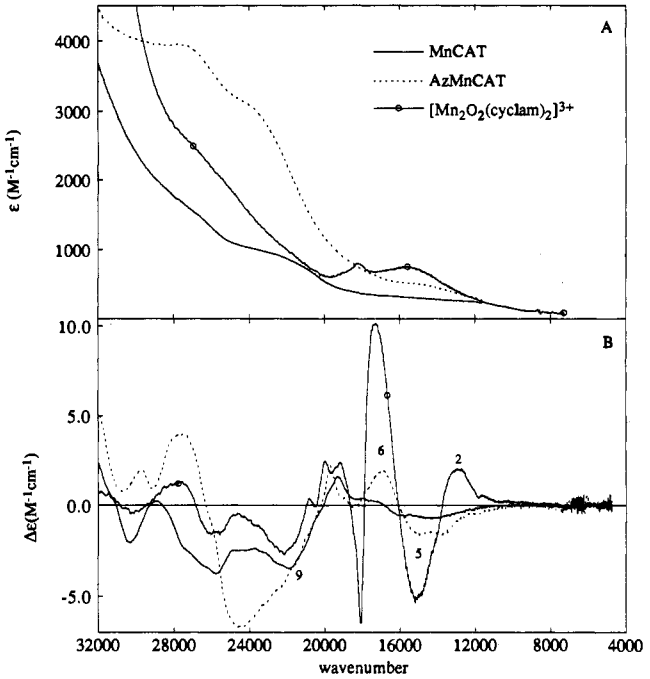

Figure 8. (A) Room-temperature solution absorption and (B) 1.8 K, 5.75 T MCD comparison of MnCAT, azide perturbed MnCAT, and $[Mn_2O_2(cyclam)_2]^{3+}$.

Also apparent from Figure 8 are quantitative differences in the common absorption and MCD features of these systems. These quantitative differences provide further structural insight into the superoxidized site of MnCAT and can be understood through correlation to model systems. The ϵ value for MnCAT from Figure 8a is 320 M^{-1} cm^{-1} at ~16 100 cm^{-1}, well below the range reported for planar complexes in this region. This is the lowest reported ϵ in this region for any di-μ-oxo [$Mn^{III}Mn^{IV}$] dimer.[30] Since MCD spectroscopy has allowed the correlation of these intensities by verifying the common electronic structural features, this suggests that the superoxidized site of MnCAT is a bent, possibly tribridged di-μ-oxo [$Mn^{III}Mn^{IV}$] dimer. This is consistent with the relatively short Mn···Mn separation of 2.67 Å observed in EXAFS.[8b] It should be noted, however, that the 2.67 Å distance alone does not exclude the possibility of a planar system, as planar di-μ-oxo [$Mn^{III}Mn^{IV}$] dimers have been reported with Mn···Mn separations ranging from 2.643[12j] to 2.750 Å,[12c] while acetate bridged di-μ-oxo dimer separations range from 2.591[12d] to 2.667 Å.[12k] A tribridged structure in the superoxidized site would also be consistent with the previous suggestion that the [$Mn^{III}Mn^{III}$] site is a μ-oxo di-μ-carboxylato dimer.[11a,13] Such dimers have been shown[11a,13] to disproportionate in aqueous solution forming di-μ-oxo μ-carboxylato [$Mn^{III}Mn^{IV}$] dimers. The di-μ-oxo [$Mn^{III}Mn^{IV}$] structure is energetically very stable, however, and may be the expected oxidation product of a variety of III,III dimers under similar conditions.

The addition of azide has been found to perturb the EPR signal of superoxidized MnCAT and result in an ~2% decrease in Mn hyperfine coupling.[2] Electronic absorption and MCD spectroscopies allow direct observation of the perturbation's effects on the superoxidized site (Figure 8) and show that azide binding results in a significant increase in intensity of the low-energy features ($\epsilon_{15200cm^{-1}} = 510\ M^{-1}\ cm^{-1}$) as well as in general intensity, while maintaining the features characteristic of a di-μ-oxo [$Mn^{III}Mn^{IV}$] dimer. From the model presented above, this suggests that the perturbation may involve a decrease in core bending, perhaps through disruption of a third bridging ligand.

(30) While MnCAT is believed to have more nonbridging oxygen ligands than the models,[10] this perturbation would increase both energies and intensities of oxo → Mn^{IV} CT transitions and would not account for the observed differences. Additionally, the low observed ϵ values cannot be attributed to a five-coordinate perturbation on the Mn^{IV}, as this would not only reduce oxo → Mn^{IV} CT intensities but would also significantly decrease CT energies.

Summary

Through a combination of electronic absorption, MCD, and resonance Raman spectroscopies a detailed understanding of the electronic spectral features associated with di-μ-oxo [$Mn^{III}Mn^{IV}$] dimers has been developed and applied to interpret the electronic spectra of superoxidized MnCAT. MCD in particular proves an invaluable tool for probing Mn cluster interactions, both in models and biological systems. These systems display a complex series of electronic transitions which directly reflect the unique aspects of metal–ligand bonding associated with the di-μ-oxo core. By studying a series of model dimers perturbed through alteration of ancillary and bridging ligation, these features are assigned, and their variation is related to the known structural perturbations of this series. Quantitative spectral differences between models in this series and throughout the literature indicate that the addition of an acetate bridge and the concomitant core bending of ~20° result in a reduction of visible absorption intensity. A molecular orbital model is presented to demonstrate the effects of core bending on Mn–oxo overlap and additionally provides insight into the orbital nature of di-μ-oxo dimer superexchange interactions. This model indicates that core bending induces a decrease in overlap of those orbitals principally responsible for visible absorption intensity in these dimers.

The understanding gained through model studies allows a comparison of these dimers' spectral features to those observed in MnCAT and azide-perturbed MnCAT. These systems exhibit characteristic features assigned to the Mn_2O_2 core, demonstrating the presence of a di-μ-oxo [$Mn^{III}Mn^{IV}$] site in superoxidized MnCAT which is perturbed by azide. Quantitative intensity differences between the model and enzyme spectra further suggest this core is bent, possibly with an additional bridge present, and that azide perturbation decreases the magnitude of this nonplanarity.

This study represents the first application of MCD spectroscopy to polynuclear manganese models and protein sites and demonstrates the utility of this technique, particularly when combined with absorption and resonance Raman spectroscopies, in developing a detailed understanding of excited-state electronic structure in these complex systems. Its application to MnCAT has allowed for electronic and geometric insight into this metalloenzyme and provides a basis for future studies on this and other manganese cluster active sites.

Acknowledgment. We thank the NSF Biophysics program (MCB9316768 to E.I.S.) and NIH (GM38275 to W.H.A. and GM45205 to J.E.P.-H.) for support of this research and the NSF (CHE9002628 to M.L.K.) for a postdoctoral fellowship.

Supplementary Material Available: Gaussian fits and fitting parameters of all MCD spectra and of the absorption fit of Figure 4a (4 pages). This material is contained in many libraries on microfiche, immediately follows this article in the microfilm version of the journal, and can be ordered from the ACS; see any current masthead page for ordering information.